10. Kitagawa, H. & van der Plicht, J. Atmospheric radiocarbon calibration to 45,000 yr B. P.: late glacial fluctuations and cosmogenic isotope production. *Science* **279,** 1187–1190 (1998).
11. Björck, S. *et al.* Synchronised terrestrial-atmospheric deglacial records around the North Atlantic. *Science* **274,** 1155–1160 (1996).
12. Stocker, T. F. & Wright, D. G. Rapid changes in ocean circulation and atmospheric radiocarbon. *Paleoceanography* **11,** 773–795 (1996).
13. Goslar, T. *et al.* Climate-related variations in the composition of the late glacial and early Holocene sediments of Lake Perespilno (eastern Poland). *Quat. Sci. Rev.* **18,** 899–911 (1999).
14. Stuiver, M. *et al.* INTCAL98 Radiocarbon age calibration, 24,000-0 cal BP. *Radiocarbon* **40,** 1041–1083 (1998).
15. Spurk, M. *et al.* Revisions and extension of the Hohenheim oak and pine chronologies: new evidence about the timing of the Younger Dryas/Preboreal transition. *Radiocarbon* **40,** 1107–1116 (1998).
16. Bard, E., Hamelin, B., Fairbanks, R. G. & Zindler, A. Calibration of the ^{14}C timescale over the past 30,000 years using mass spectrometric U-Th ages from Barbados corals. *Nature* **345,** 405–410 (1990).
17. Johnsen, S. J. *et al.* Irregular glacial interstadials recorded in a new Greenland ice core. *Nature* **359,** 311–313 (1992).
18. Hammer, C. U. *et al. The Stratigraphic Dating of the GRIP Ice Core.* (Special Report of the Geophysics Department, Inst. Niels Bohr for Astronomy, Physics and Geophysics, Univ. Copenhagen, 1998).
19. Alley, R. B. *et al.* Abrupt increase in Greenland snow accumulation at the end of the Younger Dryas event. *Nature* **362,** 527–529 (1993).
20. Brauer, A. *et al.* High resolution sediment and vegetation responses to Younger Dryas climate change in varved lake sediments from Meerfelder Maar, Germany. *Quat. Sci. Rev.* **18,** 321–329 (1999).
21. Finkel, R. C. & Nishiizumi, K. Beryllium 10 concentrations in the Greenland Ice Sheet Project 2 ice core from 3-40 ka. *J. Geophys. Res.* **102,** 26699–26706 (1997).
22. Broecker, W. S. Paleocean circulation during the last deglaciation: A bipolar seesaw? *Paleoceanography* **13,** 119–121 (1998).
23. Blunier, T. *et al.* Timing of the Atlantic cold reversal and the atmospheric CO_2 increase with respect to the Younger Dryas event. *Geophys. Res. Lett.* **24,** 2683–2686 (1997).
24. Alley, R. B. *et al.* Changes in continental and sea-salt atmospheric loadings in central Greenland during the most recent deglaciation: Model-based estimates. *J. Glaciology* **41,** 503–514 (1995).
25. Mikolajewicz, U. *A Meltwater Induced Collapse of the "Conveyor Belt" Thermohaline Circulation and its Influence on the Distribution of $\Delta^{14}C$ and $\delta^{18}O$ in the Oceans* (Technical Report 189, Max-Planck-Inst. für Meteorologie, Hamburg, 1996).
26. Goslar, T. *et al.* High-resolution lacustrine record of the Late Glacial/Holocene transition in Central Europe. *Quat. Sci. Rev.* **12,** 287–294 (1993).
27. Broecker, W. S. *et al.* The distribution of radiocarbon in the Glacial Ocean. *Glob. Biogeochem. Cycles* **4,** 103–117 (1990).

Supplementary information is available on *Nature*'s World-Wide Web site (http://www.nature.com) or as paper copy from the London editorial office of *Nature*.

Acknowledgements

We thank R. Finkel for the numerical data on ^{10}Be concentration in the GISP2 ice core, R. Alley for the data on the GISP2 accumulation rate, K. Hughen for the ^{14}C calibration data and the grey-scale record of the Cariaco sediments, S. Johnsen and C. Hammer for the data on the GRIP timescale, M. Spurk for the data on the German pine tree-ring thickness, and E. Bard for comments on the manuscript. The sediment cores from Lake Gościąż and Lake Perspilno were raised with the help of J. Pawlyta, A. Rakowski and A. Walanus. The terrestrial macrofossils were picked up by D. Moszyńska-Moskwa. The French Centre National de la Recherche Scientifique et Commissariat de l'Energie Atomique carried out accelerator mass spectrometer (AMS) ^{14}C measurements. This work has been sponsored by the Polish Committee for Scientific Research, through the grant to T.G.

Correspondence and requests for materials should be addressed to T.G. (e-mail: goslar@zeus.polsl.gliwice.pl).

A thermodynamic explanation for black smoker temperatures

Tim Jupp & Adam Schultz

Institute of Theoretical Geophysics, Department of Earth Sciences, University of Cambridge, Cambridge CB2 3EQ, UK

There is a remarkable difference between the maximum temperature of black smoker effluent (350 °C–400 °C) and the temperature of the solidifying magma which heats it (~1,200 °C)[1–3]. It has been suspected[4] for some time that the nonlinear thermodynamic properties of water[5] might be responsible for this discrepancy. Here, we translate this hypothesis into a physical model, by examining the internal temperature structure of convection cells in a porous medium. We demonstrate that, at pressures appropriate to seafloor crust, plumes of pure water form naturally at ~400 °C for any heat source with temperature greater than ~500 °C. Higher temperatures are confined to a boundary layer at the base of the convection cell, where the flow is horizontal. The phenomenon is explained analytically using the thermodynamic properties of water, and is illustrated by numerical simulations. Our model predicts the existence of the high-temperature 'reaction zone' found in ophiolites[6] and suggests that vent temperatures will remain steady as magma chambers solidify and cool[7].

Three mechanisms to limit black smoker temperatures have been proposed. The first suggestion is that high-temperature rock (greater than, say, 500 °C) is effectively impermeable, because its ductile nature prevents the formation of cracks[8,9]. The second is that high-temperature rock becomes impermeable over time, either by mineral precipitation[4,10], or by thermal expansion[11]. The third hypothesis is that the temperature cap is imposed by the thermodynamic properties of water. The first two mechanisms work by restricting flow to sufficiently cool regions of the crust. In contrast, the third mechanism allows fluid to flow at all temperatures within the crust, but limits the temperature of the fluid expelled at the sea floor.

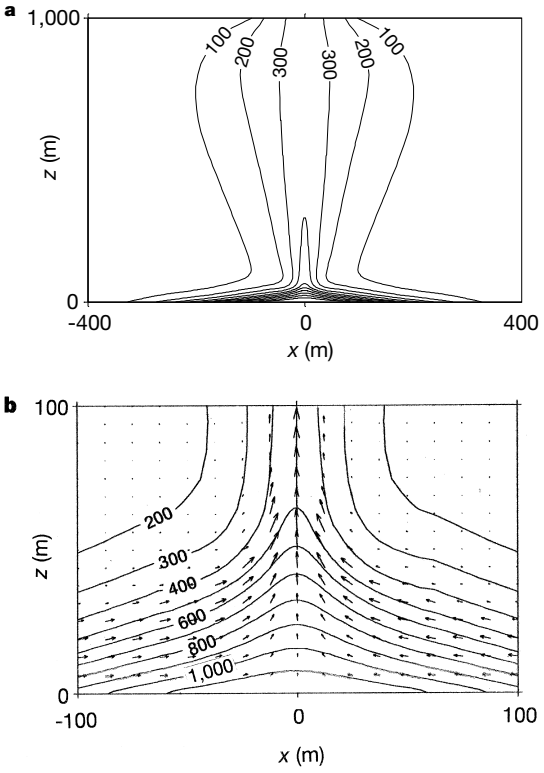

Figure 1 The steady-state temperature distribution in a convection cell at sea floor pressures. The top boundary ($z = 1{,}000$ m) represents the seafloor and is permeable. Here, the pressure is held at 25 MPa (equivalent to ~2.5 km below the sea surface). The temperature boundary condition is $T = 10$ °C where flow is downwards, and $\partial T/\partial z = 0$ where flow is upwards. The side boundaries for the simulation are at $x = -1{,}700$ m and $x = 1{,}700$ m (beyond the range of these figures), sufficiently distant that they do not influence the solution near the heater. They are held at $T = 10$ °C and cold hydrostatic pressure. The bottom boundary ($z = 0$) is impermeable. A gaussian (bell-shaped) temperature profile is imposed, representing a magma chamber. The temperature on $z = 0$ runs from 'cold' (10 °C) at the sides to 'hot' (1,200 °C) in the centre. Parameters for the simulation are a porosity of 10%, permeability $k = 10^{-14}$ m^2, thermal conductivity $\lambda = 2.0$ W m^{-1} K^{-1}. **a**, The overall temperature structure of the convection cell, showing the distinction between the boundary layer and the plume. Isotherms from 100 °C to 1,100 °C are drawn, in increments of 100 °C. Flow vectors are omitted for clarity. Flow is downwards at the sides, towards the centre at the base and upwards in the centre. **b**, A close-up view of the flow regime and temperature structure inside the boundary layer, showing the bottom 100 m of the domain. Isotherms from 200 °C to 1,100 °C are drawn, in increments of 100 °C. Vectors are of Darcy velocity.

Previous studies have shown how the thermodynamic properties of water affect the onset of convection[12] and the overall rate of heat transfer[13,14] in convection cells operating across a small temperature difference (~10 °C). Given a fixed temperature difference, convection cells operating near the critical point of water (~22 MPa, ~374 °C) transfer heat much more rapidly than cells at other temperatures. Such 'superconvection' suggests that hydrothermal systems should be able to transfer heat effectively, but it is insufficient to explain the limit to vent temperatures. Real systems operate between ~10 °C and ~1,200 °C—a large temperature difference—and vent at a particular temperature (~400 °C). To explain this, we investigate the internal temperature structure of the cell rather than the overall heat transfer.

A numerical simulation can be used to illustrate the thermal structure of convection cells[15] (Fig. 1). This simulation uses parameter values appropriate to seafloor systems. However, analysis of the governing equations shows that the main feature of the temperature structure depends solely on the thermodynamics of water, and not on the details of the parameterization. To isolate the phenomenon under discussion, all previously suggested temperature-limiting mechanisms are excluded, and the crust is taken to be homogeneous and isotropic. Simulations were performed with the software package HYDROTHERM[16] (available at http://water.usgs.gov/software/hydrotherm.html), modified to enforce a thermal boundary condition that is relevant to seafloor systems[17]. (Hot effluent emerges from an otherwise cold seafloor, so a fixed-temperature boundary condition is not always appropriate. Consequently, the condition $\partial T/\partial z = 0$ is imposed on the sea floor where flow is upwards, and $T = 10\,°C$ is imposed where flow is downwards).

The governing equations are Darcy's law[18], an equation of state for pure water[19–22] and the conservation of mass and energy in a porous medium[18]. Convection is initiated by a 'heater' along part of the bottom boundary[23], which represents the top of a magma chamber. For simplicity, the heater imposes a gaussian (bell-shaped) temperature profile which runs from 'cold' (T_0) at the sides to 'hot' ($T_0 + \Delta T$) at the centre. The heater is 'switched on' at time zero, when the domain is cold ($T = T_0$) and at hydrostatic pressure. Time-dependent solutions for the temperature and pressure fields are calculated and allowed to evolve until a steady state is reached.

A typical steady-state solution with $T_0 = 10\,°C$ and $(T_0 + \Delta T) = 1{,}200\,°C$ is shown in Fig. 1. There is a thin boundary layer of very hot fluid (500 °C to 1,200 °C) at the base of the convection cell. This layer, in which flow is horizontal, can be compared with the 'reaction zone' observed in ophiolites, for which similar temperatures have been inferred[6]. The temperature of the plume is about 400 °C. Similar plume temperatures were obtained for other systems dominated by convection, with $T_0 = 10\,°C$ and $(T_0 + \Delta T) >$ ~500 °C, including systems with anisotropic permeability. It follows that vent temperatures could remain steady as a magma chamber solidified and cooled, dropping only when the heat source fell below ~500 °C.

It appears that plumes have a natural tendency to form at ~400 °C, given a sufficient heat source and seafloor pressures. The explanation for this phenomenon lies in the balance between conduction and advection—the two mechanisms which transport energy in a convection cell.

In the model (Fig. 1), the temperature T and pressure p are functions of position $\mathbf{x} = (x,z)$. Thermal gradients produce a conductive heat flux $-\lambda\nabla T$, where λ is the thermal conductivity. Fluid motion creates an advective heat flux $\rho h\mathbf{u}$, for water of density ρ, specific enthalpy h and Darcy velocity $\mathbf{u}$. In the conservation of energy equation[18], the rate of change of energy per unit volume is given by the negative divergence of the total heat flux, or $-\nabla\cdot(\rho h\mathbf{u} - \lambda\nabla T)$. This can be split into two terms, $-\nabla\cdot(\rho h\mathbf{u})$ and $\lambda\nabla^2 T$, which are rates of accumulation of energy per unit volume, due to advection and conduction respectively. At any point in the cell, the relative importance of these two mechanisms can be expressed by the ratio $Ra_L(\mathbf{x}, t) = |\nabla\cdot(\rho h\mathbf{u})/\lambda\nabla^2 T|$. This ratio measures the influence of fluid motion on the evolution of the local temperature field, and could logically be labelled the 'local Rayleigh number'. (Traditionally, a single parameter—the 'Rayleigh number'—is defined for the whole cell[12]. Here, a 'local Rayleigh number' has been assigned, independently, to each point in the cell.) If $Ra_L \ll 1$, conduction dominates over advection, and the temperature evolves independently of any fluid flow. Conversely, where $Ra_L \gg 1$, advection is strong enough to influence the temperature field, and the isotherms can be distorted away from a pattern dominated by conduction. Advective distortion of the isotherms marks the separation of the plume from the boundary layer—indeed, it is what defines the plume on a plot of the temperature field (Fig. 1). To discover where plumes will appear, it is important to know where Ra_L is largest.

After the heater is switched on, a thermal signal propagates upwards (Fig. 2). For the period before plume formation (Fig. 2a and b), the approximate magnitudes of the energy accumulation terms can be calculated. Let d be the distance that the signal has penetrated into the domain, that is, the vertical range over which the temperature drops from 'hot' ($T_0 + \Delta T$) to 'cold' (T_0). Suppose that $|\rho h\mathbf{u}|$ is of order Φ. Hence $|\nabla\cdot(\rho h\mathbf{u})|$ is of order Φ/d, and $|\lambda\nabla^2 T|$ is of order $\lambda\Delta T/d^2$. Consequently, Ra_L is of order $(\Phi/\lambda\Delta T)\cdot d$, and so

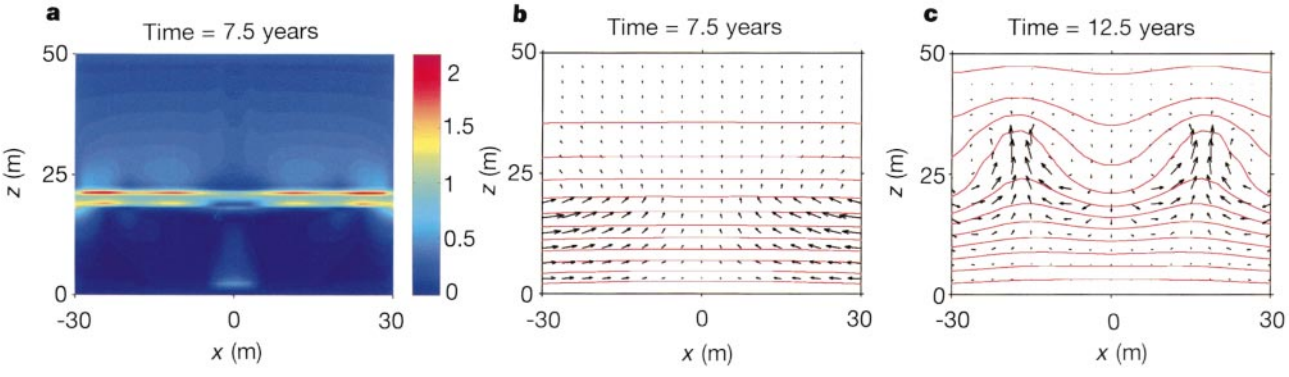

Figure 2 Early stages of the simulation, at the bottom of the domain shown in Fig. 1. **a**, Colour plot of the local Rayleigh number Ra_L, before plume formation. The regions of greatest Ra_L indicate where plumes are likely to form. **b**, The temperature and flow fields before plume formation. The thermal structure is governed by conduction alone. Convective motion exists, but it does not influence the temperature field. **c**, The temperature and flow fields after plume formation. Advection has begun to distort the thermal structure. (As the simulation progresses to steady state, these two plumes coalesce to form the single plume in Fig. 1.) Isotherms are drawn from 100 °C (top) to 1,100 °C (bottom) in increments of 100 °C. Vectors are of Darcy velocity.

scales linearly with the vertical length scale d. Just before plume formation, d is sufficiently small that Ra_L is everywhere of order unity (Fig. 2a). Note that Ra_L is greatest near the 400 °C isotherm. A short time later, when d, and hence Ra_L, have increased slightly, plumes appear at about 400 °C (Fig. 2c).

By making some simplifications, it is possible to estimate the temperature at which Ra_L is maximized, just before plume formation. Temperature gradients are nearly uniform (Fig. 2b). It follows that the maximum value of Ra_L is controlled by the maximum value of $|\nabla\cdot(\rho h\mathbf{u})|$. By analogy with convection in a U-shaped pipe[24], a convection cell can be divided into a cold 'downflow limb' and a hot 'upflow limb'. The vertical pressure gradient must be sufficiently small for cold water to flow down the downflow limb, and sufficiently large for hot water to flow up the upflow limb. Hence, the pressure gradient lies between hot hydrostatic and cold hydrostatic. The permeability is the same in both limbs, but the total resistance to flow is much greater in the upflow limb because of its smaller cross-sectional area (Fig. 1). It follows that the pressure gradient will be much closer to cold hydrostatic than hot hydrostatic. Hence $\partial p/\partial z \approx -\rho_0 g$, where ρ_0 is the density of cold water. Suppose that the advective heat flux $\rho h\mathbf{u}$ is dominated by its vertical component, which by Darcy's law[18] is $-k(\partial p/\partial z + \rho g)\rho h/\mu$, for permeability k, gravitational acceleration g, and dynamic viscosity μ. An approximate expression for the advective energy accumulation is then:

$$-\nabla\cdot(\rho h\mathbf{u}) \approx \left[\frac{\partial}{\partial z}\left(\frac{(\rho_0-\rho)\rho h}{\mu}\right)\right]\cdot[-gk]$$

Denoting $(\rho_0 - \rho)\rho h/\mu$ by F, it follows that Ra_L should be maximized where $|\partial F/\partial z|$ is maximized. The quantity F has been termed 'fluxibility'[1] and measures the ability of buoyancy-driven water to transport energy. Fluxibility is a function of the thermodynamic state of the water (ρ_0 is constant and ρ, μ and h are known as functions of pressure and temperature from steam tables[19–22]). Figure 3a shows how fluxibility depends on pressure and temperature over an appropriate range. In a seafloor hydrothermal system, the fluxibility varies greatly with temperature, but little with pressure. Before the formation of a plume, temperature is approximately a linear function of height (Fig. 2b). Thus, $|\partial F/\partial z|$ should be maximized roughly where $|\partial F/\partial T|$ is maximized.

Figure 3c shows clear peaks in $|\partial F/\partial T|$ at ~384 °C (p = 25 MPa) and ~412 °C (p = 35 MPa). These are the temperatures at which plumes would separate from the boundary layer under the simplifying assumptions. They are remarkably close to the plume temperatures in the numerical simulation (Fig. 1a and b, Fig. 2c).

This analysis uses the properties of pure water, because values of ρ, μ and h are not available for salt water over all of the required temperature range[4,25]. When such data become available, the calculation should be repeated for salt water. It seems likely[4] that the peaks in the $|\partial F/\partial T|$ curves would be shifted to higher temperatures by about 30 °C. Nonetheless, the use of pure water has one definite advantage. At pressures greater than 22 MPa (seafloor depth ~2.2 km), pure water is a single-phase fluid. Hence, the complication of phase separation has been removed from this analysis, and it has been possible to demonstrate a temperature-limiting mechanism that is independent of 'phase-separation' or 'two-phase effects'.

Three differences between this approach and classical studies of porous medium convection[26] should be noted. First, convection is not here generated by a uniformly heated lower boundary. The presence of both 'hot' and 'cold' at the base of the cell ensures that there is always a horizontal temperature gradient and associated fluid flow. The point of interest is not the onset of convective motion, but the onset of convective distortion of the temperature field. Second, no use is made of the Boussinesq approximation[27], under which the advective heat flux would be simplified to $\rho_0 h\mathbf{u}$. The true value $\rho h\mathbf{u}$ is used here because ρ can vary from ρ_0 by a factor of 25. Thirdly, this analysis abandons the traditional Rayleigh number[27], which is an overall balance between advection and conduction, in favour of a local Rayleigh number giving the balance at each point in the cell. This permits a discussion of the precise position (equivalently, temperature) at which plumes form.

At a given pressure, and given a sufficient source of heat, a plume is likely to form at the temperature of maximum fluxibility gradient (Fig. 3c). Hence, if ambient pressures are known, plume formation temperatures could be inferred for single-phase hydrothermal systems. Vents may be cooler than this plume-formation temperature because of conductive losses from the ascending fluid, but they cannot be hotter. □

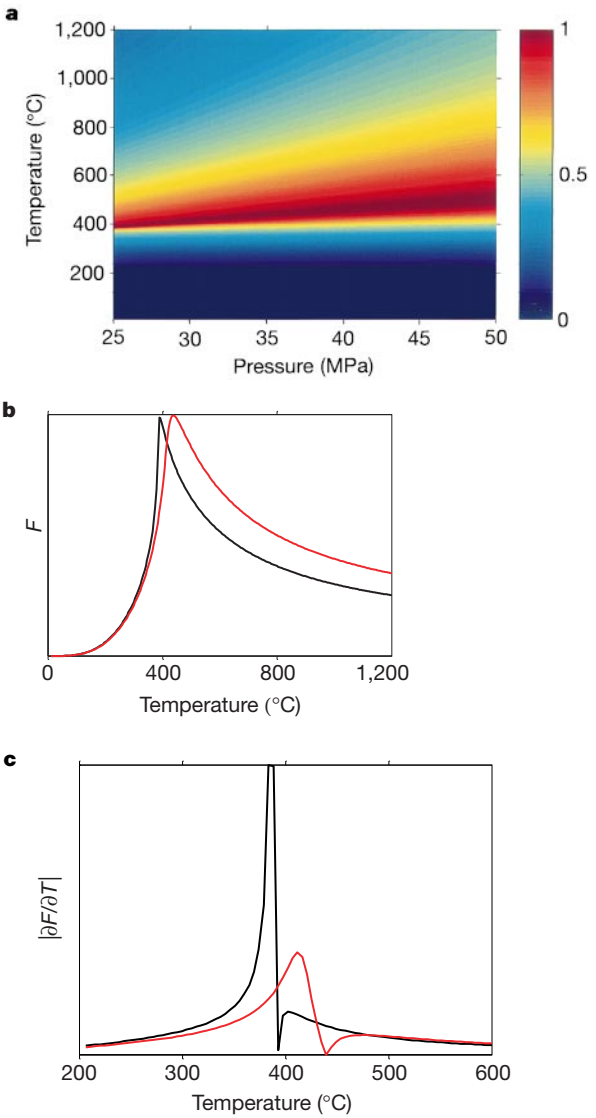

Figure 3 'Fluxibility' F and 'fluxibility gradient' $|\partial F/\partial T|$ (in normalized units) **a**, F as a function of temperature T and pressure p. The pressure range of 25 MPa to 50 MPa (~2.5 km to ~5 km cold hydrostatic head) is representative of the pressures found in seafloor hydrothermal systems. **b**, F as a function of T at p = 25 MPa (black line) and p = 35 MPa (red line). These pressures are lower and upper bounds for the pressures to be found in the cell in Fig. 1. **c**, $|\partial F/\partial T|$ as a function of T at p = 25 MPa (black line) and p = 35 MPa (red line). The temperature at which $|\partial F/\partial T|$ is maximized is, approximately, the temperature at which plumes form.

Received 6 May; accepted 9 December 1999.

1. Lister, C. R. B. Heat transfer between magmas and hydrothermal systems, or, six lemmas in search of a theorem. *Geophys. J. Int.* **120,** 45–59 (1995).
2. Lowell, R. P., Rona, P. A. & Von Herzen, R. P. Seafloor hydrothermal systems. *J. Geophys. Res.* **100,** 327–352 (1995).
3. Wilcock, W. S. D. Cellular convection models of mid-ocean ridge hydrothermal circulation and the

temperatures of black smoker fluids. *J. Geophys. Res.* **103,** 2585–2596 (1998).
4. Bischoff, J. L. & Rosenbauer, R. J. An empirical equation of state for hydrothermal seawater (3. 2 percent NaCl). *Amer. J. Sci.* **285,** 725–763 (1985).
5. Johnson, J. W. & Norton, D. Critical phenomena in hydrothermal systems: state, thermodynamic, electrostatic, and transport properties of H_2O in the critical region. *Am. J. Sci.* **291,** 541–648 (1991).
6. Gillis, K. M. & Roberts, M. D. Cracking at the magma-hydrothermal transition: evidence from the Troodos Ophiolite, Cyprus. *Earth Planet. Sci. Lett.* **169,** 227–244 (1999).
7. Lowell, R. P. & Germanovich, L. N. On the temporal evolution of high-temperature hydrothermal systems at ocean ridge crests. *J. Geophys. Res.* **99,** 565–575 (1994).
8. Lister, C. R. B. On the penetration of water into hot rock. *Geophys. J. R. Astron. Soc.* **39,** 465–509 (1974).
9. Fournier, R. O. The transition from hydrostatic to greater than hydrostatic fluid pressure in presently active continental hydrothermal systems in crystalline rock. *Geophys. Res. Lett.* **18,** 955–958 (1991).
10. Lowell, R. P., Van Cappellen, P. & Germanovich, L. Silica precipitation in fractures and the evolution of permeability in hydrothermal upflow zones. *Science* **260,** 192–194 (1993).
11. Germanovich, L. N. & Lowell, R. P. Percolation theory, thermoelasticity, and discrete hydrothermal venting in the Earth's crust. *Science* **255,** 1564–1567 (1992).
12. Straus, J. M. & Schubert, G. Thermal convection of water in a porous medium: effects of temperature- and pressure-dependent thermodynamic and transport properties. *J. Geophys. Res.* **82,** 325–333 (1977).
13. Dunn, J. C. & Hardee, H. C. Superconvecting geothermal zones. *J. Volcanol. Geotherm. Res.* **11,** 189–201 (1981).
14. Ingebritsen, S. E. & Hayba, D. O. Fluid flow and heat transport near the critical point of H_2O. *Geophys. Res. Lett.* **21,** 2199–2202 (1994).
15. Norton, D. & Knight, J. Transport phenomena in hydrothermal systems: cooling plutons. *Am. J. Sci.* **277,** 937–981 (1977).
16. Hayba, D. O. & Ingebritsen, S. E. *The Computer Model HYDROTHERM, a Three-dimensional Finite-difference Model to Simulate Ground-water Flow and Heat Transport in the Temperature Range of 0 to 1,200 degrees Celsius.* (US Geological Survey Water-Resources Investigations Report, 94-4045, Denver, Colorado, 1994).
17. Dickson, P., Schultz, A. & Woods, A. in *Hydrothermal Vents and Processes* (ed. Parson, L. M. *et al.*) Vol. 87, 145–157 (Geological Society Special Publication, London, 1995).
18. Faust, C. R. & Mercer, J. W. Geothermal reservoir simulation 1. Mathematical models for liquid- and vapor-dominated hydrothermal systems. *Wat. Resour. Res.* **15,** 23–30 (1979).
19. Haar, L., Gallagher, J. S. & Kell, G. S. *NBS/NRC Steam Tables,* 1–320 (Hemisphere, New York, 1984).
20. Watson, J. T. R., Basu, R. S. & Sengers, J. V. An improved representative equation for the dynamic viscosity of water substance. *J. Phys. Chem. Ref. Data* **9,** 1255–1290 (1980).
21. Sengers, J. V. & Kamgar-Parsi, B. Representative equations for the viscosity of water substance. *J. Phys. Chem. Ref. Data* **13,** 185–205 (1984).
22. Sengers, J. V. & Watson, J. T. R. Improved international formulation for the viscosity and thermal conductivity of water substance. *J. Phys. Chem. Ref. Data* **15,** 1291–1314 (1986).
23. Elder, J. E. *Geothermal Systems* 180–187 (Academic, London, 1981).
24. Pascoe, A. R. & Cann, J. R.in *Hydrothermal Vents and Processes* (ed. Parson, L. M. *et al.*) Vol. 87, 159–173 (Geological Society Special Publication, London, 1995).
25. Anderko, A. & Pitzer, K. S. Equation-of-state representation of phase equilibria and volumetric properties of the system NaCl-H_2O above 573 K. *Geochim. Cosmochim. Acta.* **57,** 1657–1680 (1993).
26. Lapwood, E. R. Convection of a fluid in a porous medium. *Proc. Camb. Phil. Soc.* **44,** 508–521 (1948).
27. Phillips, O. M. *Flow and Reactions in Permeable Rocks* 245–264 (Cambridge Univ. Press, 1991).

Acknowledgements

We thank USGS for permission to use HYDROTHERM. The calculations were carried out on the Enigma high-performance computing centre at the Institute of Theoretical Geophysics. We acknowledge the support of that facility by the Higher Education Research Foundation for England. T.J. is supported by a studentship from the Natural Environment Research Council.

Correspondence and requests for materials should be addressed to T.J. (e-mail: tim@itg.cam.ac.uk).

An interconnected network of core-forming melts produced by shear deformation

D. Bruhn, N. Groebner & D. L. Kohlstedt

Department of Geology & Geophysics, University of Minnesota, Minneapolis, Minnesota 55455, USA

The formation mechanism of terrestrial planetary cores is still poorly understood, and has been the subject of numerous experimental studies[1–3]. Several mechanisms have been proposed by which metal—mainly iron with some nickel—could have been extracted from a silicate mantle to form the core. Most recent models involve gravitational sinking of molten metal or metal sulphide through a partially or fully molten mantle[4,5] that is often referred to as a 'magma ocean'. Alternative models invoke percolation of molten metal along an interconnected network (that is, porous flow) through a solid silicate matrix[6,7]. But experimental studies performed at high pressures[1–3] have shown that, under hydrostatic conditions, these melts do not form an interconnected network, leading to the widespread assumption that formation of metallic cores requires a magma ocean. In contrast, here we present experiments which demonstrate that shear deformation to large strains can interconnect a significant fraction of initially isolated pockets of metal and metal sulphide melts in a solid matrix of polycrystalline olivine. Therefore, in a dynamic (non-hydrostatic) environment, percolation remains a viable mechanism for the segregation and migration of core-forming melts in a solid silicate mantle.

Percolation of core-forming melts by porous flow through a silicate matrix has until now been largely been ruled out as a possible melt segregation mechanism: this has been on the basis of microstructural observations of the distribution of metal sulphide melts in silicate samples that were hydrostatically annealed at high pressures and temperatures[1–3]. Such observations of melt–solid microstructures are commonly interpreted in terms of the dihedral angle θ, the angle between two neighbouring grains of the solid matrix in contact with melt. This angle is determined by the value of the solid–melt interfacial energy, γ_{sm}, relative to the value of the solid–solid interfacial energy, γ_{ss}, according to the relation:

$$\gamma_{sm}/\gamma_{ss} = 2\cos(\theta/2)$$

For $\theta > 60°$ (that is, large relative values of the solid–melt interfacial energy), the melt does not wet triple junctions, so that percolation is impossible unless the melt fraction exceeds a critical value that increases with increasing dihedral angle[8]. For $0 < \theta < 60°$, the melt phase forms an interconnected network along triple junctions, even at small melt fractions, such that complete drainage of melt by percolation through the solid matrix is possible.

The argument against percolation as a core-forming mechanism is based on the observation that the dihedral angle for metal sulphide melt in the silicate matrix is greater than 60° (refs 1–3). In these high-pressure studies, powders similar in composition to the mantle (that is, olivine with the addition of iron and nickel and iron–nickel sulphides) and powders of a chondritic meteorite believed to be similar in composition to the primitive mantle of Earth were subjected to pressures ranging from 2 to 20 GPa and temperatures of 1,210 to 1,710 °C; these temperatures are higher than the melting point of the metal alloys and metal sulphides, but below the melting point of olivine. Dihedral angles ranged from 70° to 125°; this shows that the metallic melt is not interconnected, as long as the melt fraction does not exceed a critical value.

For a metallic melt content greater than this critical value in the early Earth, the melt would have been interconnected; melt would have drained to the core until the critical melt fraction was reached in the mantle. At this point, drainage would have ceased, stranding the remaining metallic melt. In theory, the critical melt content is ~6 vol.% (for a dihedral angle of 100°)[4,8], whereas electrical conductivity experiments place the critical melt content for the olivine–iron system at 10–25% (ref. 9). These values are much larger than the amount of metal stranded in the present-day Earth's mantle[10]. In view of the large values measured for the dihedral angle, several authors have concluded that percolation is not a feasible mechanism for the extraction of core-forming melts from the mantle[1–3]. Consequently, they argue that a significant degree of silicate melting is required to efficiently segregate metal-rich melt from a silicate matrix.

The limitation of this conclusion is, as pointed out by Stevenson[4], that it is based on experiments carried out under hydrostatic conditions. In contrast, an evolving mantle would not be static,